Materials Science & Engineering A 730 (2018) 1–9

Contents lists available at ScienceDirect

Materials Science & Engineering A

journal homepage: www.elsevier.com/locate/msea

Impact toughness of a 10% Cr steel with high boron and low nitrogen contents

R. Mishnev, N. Dudova*, V. Dudko, R. Kaibyshev

Belgorod State University, Pobeda 85, Belgorod 308015, Russia

ARTICLE INFO

Keywords:
Fracture
Brittle-to-ductile transition
Charpy impact test
Martensitic steel
Fractography

ABSTRACT

The effect of temperature on the impact toughness and fracture behavior of a 10% Cr-2% W-0.7% Mo-3% Co-0.05% Nb-0.2% V-0.008% B-0.003% N (all in wt%) steel was studied. The ductile-brittle transition (DBT) occurs at 10 °C. At the DBT temperature (DBTT), the onset of unstable crack propagation occurs at the maximum load. The embrittlement is attributed to the onset of unstable crack propagation at stresses below the general yielding. A decrease in nitrogen content and an increase in boron content lead to the formation of chains of closely spaced $M_{23}C_6$ carbides at lath boundaries. The formation of numerous voids at carbide-matrix boundaries results in the appearance of crack with critical dimension after stable crack propagation over a very short distance. As a result, the energy of the stable crack propagation is low and the embrittlement takes place at relatively high temperature.

1. Introduction

Heat-resistant high-chromium martensitic steels are widely used in various critical components of fossil power plants due to their superior creep resistance and high-temperature strength [1,2]. High fracture toughness is an important property to assure the reliability of steam turbine parts produced from these steels [1]. The 9% Cr steels with ~0.1 wt% C and ~0.05 wt% N exhibit a high toughness ≥ 200 J/cm^2 at room temperature [3–10]. The ductile-brittle transition temperatures (DBTTs), which are estimated on the basis of 68 J criterion or the V-notch impact energy absorption halfway between the upper and lower shelf energies, are in the low temperature intervals of − 100…− 45 and − 60…− 40 °C, respectively [5–10]. Moreover, the 28 J impact transition temperature ($T_{28\,J}$) for these steels is in the range of − 120…− 70 °C [5–9,11]. It is known that long-term aging at exploitation temperature leads to a 2–4-fold decrease in the Charpy V-notch impact energy at ambient temperature and to an increase in DBTT up to 100 °C [1,10,12–14]. When the operating or ambient temperatures are lower than DBTT, the steel may suffer catastrophic fracture and cause serious accidents. The room temperature impact toughness in these steels remains at a level above 40 J/cm^2, guaranteeing sufficiently safe operation of steam turbine parts [1].

The heat treatment of high-chromium steels consists of normalizing from $T \geq 1050$ °C and tempering at temperatures ranging from 750° to 780°C for 2–4 h and results in a tempered martensite lath structure (TMLS) composed of a hierarchical sequence of structural elements, i.e., prior austenite grains (PAGs), martensite packets, blocks, and laths with a high dislocation density [1–9,12–14]. $M_{23}C_6$ carbides with the average size of ~100 nm and nanoscale MX carbonitrides (where M is Nb or V and X is C or N) precipitate during tempering [1–5]. In these steels, DBT as revealed by the Charpy impact tests is associated with a transition between two failure modes, i.e., brittle transgranular cleavage at low temperatures and ductile fracture at elevated temperatures [5–10]. Therefore, the mechanical integrity of steam turbine components produced from high-chromium steels critically depends on flaws, which may appear either during manufacturing or during service [6,15–20]. At $T \geq T_{28\,J}$, there is a competition between the stable crack propagation occurring in a ductile manner and the unstable crack propagation with a cleavage fracture [6,16]. It is known [15–20], the brittle fracture may include both cleavage and intergranular fracture. The particles located at various boundaries may act as the crack initiation sites in high-chromium steels, although TMLS is unsusceptible for intergranular brittleness [3,6,18–20]. The intergranular crack propagation has been shown along the continuous films of boundary $M_{23}C_6$ carbides in a 9 wt% Cr steel after tempering at 500 °C, leading to a full embrittlement with an impact-absorbed energy of approximately 6 J/cm^2 [3,17]. In contrast, high-temperature tempering results in almost round shaped $M_{23}C_6$ particles and makes the boundaries of TMLS highly resistant to an intergranular fracture. In addition, these boundaries act as an effective obstacle to transgranular cleavage crack propagation due to segregations of carbon; the crossing of grain boundaries by cleavage cracks is hindered or could be arrested [16,19,20].

* Corresponding author.
E-mail address: dudova@bsu.edu.ru (N. Dudova).

https://doi.org/10.1016/j.msea.2018.05.103
Received 6 April 2018; Received in revised form 23 May 2018; Accepted 26 May 2018
Available online 27 May 2018
0921-5093/

Transgranular quasi-brittle fracture could be initiated due to shear-induced cracking of brittle boundary particles followed by the propagation of these cracks in the transgranular manner overcoming boundary barriers [18,19]. It is apparent [6] that this fracture mechanism provides a sufficient Charpy V-notch impact energy above 20 J/cm^2 at cryogenic temperatures. Full embrittlement of 9 wt% Cr steels with an impact-absorbed energy of 6 J/cm^2 occurs just after a negligible initiation stage at − 196 °C [6]. Thus, the origin of embrittlement of high-chromium steels subjected to high-temperature tempering is still unclear.

Recently, a new generation of high-boron 9–10% Cr steels exhibiting improved creep properties were developed [21–25]. The high boron content provides two-phase separation of $M_{23}C_6$ carbides into B-free $M_{23}C_6$ carbides and $M_{23}(B{\cdot}C)_6$ phase and the refinement of these particles to 70 nm [22–27]. It is known [18] that the cleavage fracture initiated by cracking of boundary particles depends on their dimensions; the cleavage fracture stress increases with a decrease in the particle diameter. However, boron segregates to the high-angle boundaries of PAGs [23] that reduce the grain boundary cohesion. The boron segregations shift the DBTT towards high temperatures and result in a strong embrittlement at low temperatures that is associated with an intergranular cracking [16]. In addition, a high level of B requires a decrease of N content below about 100 ppm to avoid the formation of boron nitrides (BN), which also lead to embrittlement [1,28]. To date, the effect of lowering the N content and increasing the B content on DBT in high-chromium steels has not been detailed. Yan et al. [29,30] have shown that the 9 wt% Cr − 3%wt W – 3 wt% Co steel with 0.013 wt% B and 0.014 wt% N exhibits the V-notch impact energy of ~100 J/cm^2 at ambient temperature and this value drops by a factor of 3 under long-term aging due to precipitation of Laves phase at boundaries. It is worth noting that the long-term aging of a P92 steel also produces a 3-fold decrease in the fracture toughness [14]. Therefore, the distribution of boundary particles is very important for impact toughness of high-chromium steels.

The aim of the present work is to study DBT in a 10% Cr steel containing high B and low N contents under impact loading. The present results will be compared with those obtained for a P92-type steel [6].

2. Experimental procedure

A 10% Cr steel with the chemical composition of 0.1% C, 0.06% Si, 0.1% Mn, 10.0% Cr, 0.17% Ni, 0.7% Mo, 0.05% Nb, 0.2% V, 0.003% N, 0.008% B, 2.0% W, 3.0% Co, 0.002% Ti, 0.006% Cu, 0.01% Al (in wt%) and Fe-balance was examined. The steel was subjected to normalizing at 1060 °C for 30 min followed by air cooling and tempering at 770 °C for 3 h. This steel has exhibited an outstanding time to rupture of about 40,000 h upon creep test at an applied load of 120 MPa at 650 °C [25]. The details of steel processing and creep tests were reported in previous works [24,25,27]. A P92-type steel was used for comparison, its chemical composition and processing details can be found elsewhere [6,31].

Standard V-notch Charpy impact specimens were tested using an Instron 450 J impact machine (Model SI-1 M) with an Instron Dynatup Impulse data acquisition system following the ASTM E-23 standard [32] at temperatures ranging from −196...100 °C.

The microstructure was examined using Jeol JEM-2100 transmission electron microscope (TEM) equipped with an INCA energy dispersive X-ray spectrometer and Quanta 600FEG scanning electron microscope (SEM) equipped with an electron backscatter diffraction (EBSD) pattern analyzer incorporating an orientation imaging microscopy (OIM) system. The OIM images were subjected to a cleanup procedure, setting the minimal confidence index to 0.1. The low- and high-angle boundaries (LABs and HABs) were defined to have misorientations of $2^\circ \le \theta < 15^\circ$ and $\ge 15^\circ$ and depicted in the OIM images using white and black lines, respectively. TEM foils were prepared by double jet electro-polishing method using a solution of 10% perchloric acid in glacial acetic acid. The transverse lath sizes were measured on the TEM micrographs by the linear intercept method counting all the clear visible (sub)boundaries. The dislocation densities were estimated by counting the individual dislocations in the (sub) grain/lath interiors. The fractured surfaces of the Charpy impact specimens were observed using a Quanta 200 SEM. The side views of unstable and stable crack propagation were analyzed on the fractured specimens of the present 10% Cr and P92-type steels just under principal crack by SEM and EBSD. The fraction of shear fracture after impact tests at different temperatures was calculated according to ASTM E 23 [32]. The volume fractions of voids were estimated by the point count technique according to ASTM E 562–02. The equilibrium volume fractions of the precipitated phases in the present 10% Cr and P92-type steels at corresponding tempering temperatures of 770 and 750 °C, respectively, were calculated by the Thermo-Calc software (Ver. 5) using the TCFE6 database. Other details of mechanical and structural characterizations were reported in previous works [6,24,25,27].

3. Results

3.1. Microstructure after normalization and tempering

TMLS of the present 10% Cr steel is shown in Fig. 1. This microstructure is typical of high-chromium martensitic steels [1,24,25,27,33,34]. An average size of PAGs is 35 μm, an average width of martensite laths is 0.4 μm, and the dislocation density is 1.7×10^{14} m^{-2}. The $M_{23}C_6$ carbides with the mean sizes of 60 nm and 100 nm locate on the lath boundaries and HABs of PAGs/packets/blocks, respectively. These carbides comprise almost continuous chains of particles. MX-type carbonitrides, mainly Nb-rich particles, with an average size of 35 nm are uniformly distributed within the martensite laths.

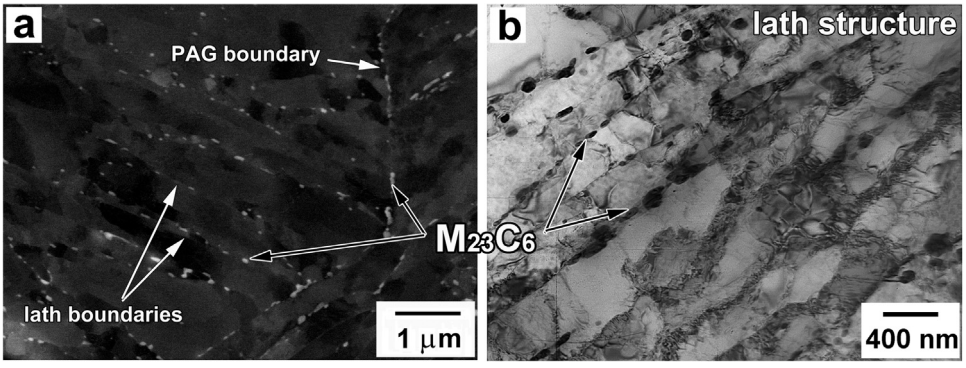

Fig. 1. SEM (back-scattered electron) (a) and bright-field TEM (b) images of the tempered martensite lath structure.

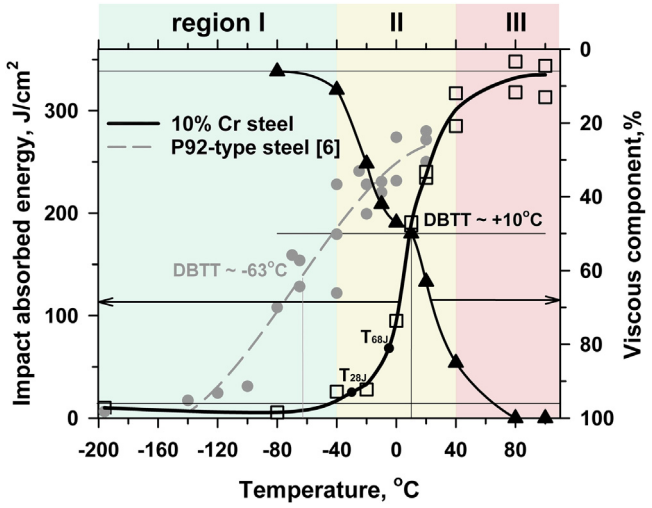

Fig. 2. Temperature dependence of the Charpy energy and the viscous fracture component for the present 10% Cr steel and a P92-type steel [6].

3.2. Impact tests

The effects of the temperature on the Charpy V-notch impact-absorbed energy and the portion of the shear fracture are presented in Fig. 2. The lower shelf region is located at temperatures below − 40 °C (the region I), the transition region is observed at temperatures from − 40–40 °C (the region II) and the upper shelf region (the region III) is located at temperatures above 40 °C. The upper shelf energy for the present 10% Cr steel is 335 J/cm^2, which is higher than that in the P92-type steel by a factor of 1.3 [6]. At room temperature, the present 10% Cr steel shows a high impact toughness of 240 J/cm^2 much similar to the P92-type steel [6].

The temperatures of DBT, which were estimated on the basis of 68 J criterion and obtained as a halfway point between the upper and lower shelf energies, are − 5 °C and 10 °C, respectively (Fig. 2). At the DBTT of 10 °C, the present 10% Cr steel exhibits high impact toughness of 185 J/cm^2. The DBTT of the present 10% Cr steel is approximately 45–100 K higher than those for the P91-, P92-, P911-type steels and the China Low Activation Martensitic (CLAM) steel [5–9,13]. In particular, the DBTT for the P92-type steel is − 63 °C [6] that is 73 K lower than for the present 10% Cr steel (Fig. 2). It should be noted that the fracture appearance transition temperature (*FATT*) corresponding to the equal fractions of the brittle and ductile components on the fracture surface [32] and the DBTT determined as a temperature corresponding to the half of the sum of the upper and lower shelf energies are the same (Fig. 2).

The 28 J transition temperature, $T_{28\,J}$, of − 27 °C is relatively high and approximately 45–100 K higher than those for P91-, P92-, P911-type and CLAM steels [5–9,13]. Full embrittlement corresponding to an impact-absorbed energy of 6 J/cm^2 appears at − 80 °C. This temperature could be termed as the 6 J impact embrittlement temperature, $T_{6\,J}$. Further decrease in temperature affects the Charpy V-notch impact-absorbed energy insignificantly. It can be concluded that lowering the N content and increasing the B contents shifts the absorbed energy–temperature curve to higher temperatures, increases the DBTT and leads to more sharp change in the absorbed energy in the transition region as compared to conventional steels with 0.05% N and approximately 0.003% B such as P92-type steel [5–9,13].

Fig. 3(a) shows the load-deflection curves obtained during the impact tests. In the transition region II and upper shelf region III, the general yield load, P_{GY}, is attained at the deflections ranging from 1.4 to 1.8 mm. The values of maximum load, P_m, are remarkably higher than the P_{GY} values. The maximum load is attained after the pendulum is displaced by about 4 mm. In the upper shelf region, any unstable crack

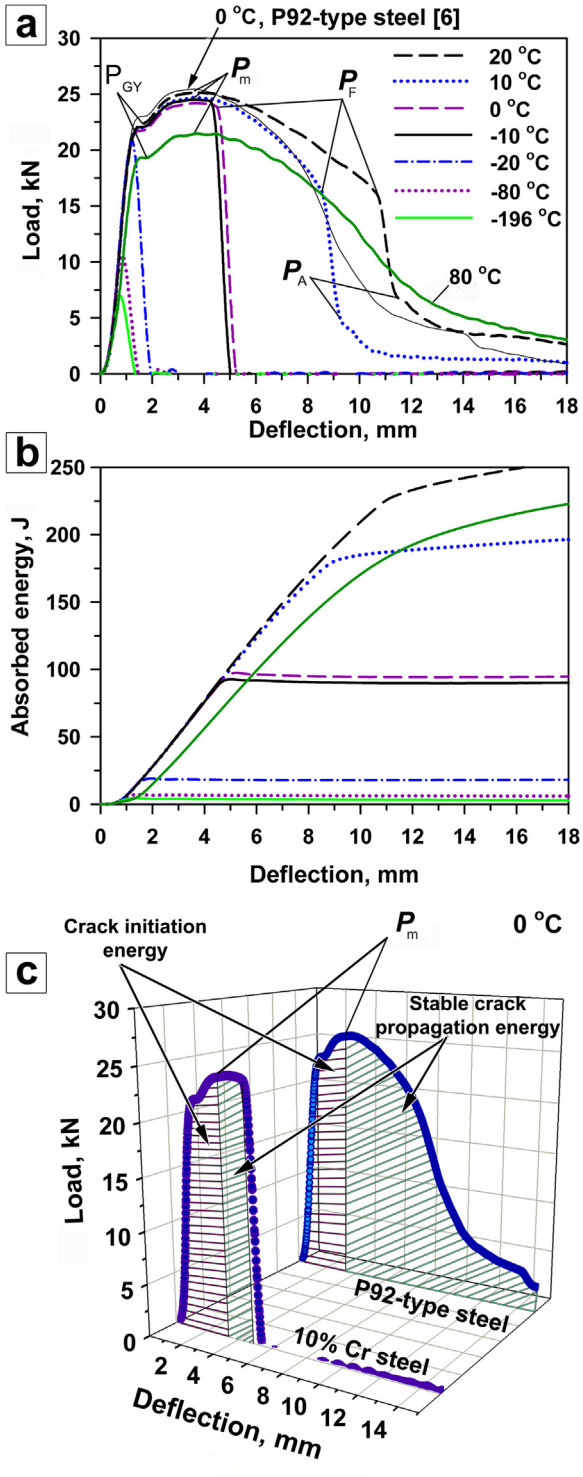

Fig. 3. Load-deflection (a, c) and absorbed energy (b) curves for the present 10% Cr steel and a P92-type steel [6] obtained under impact loading. P_{GY} is a load at general yield; P_m is a maximum load; P_F is a fracture load for general cleavage; P_A is an arrest load.

propagation is not observed. The P_m value increases with a transition from the region III to region II, whereas P_m does not depend on temperature in the region II. In the region II at temperatures above the DBTT, which is obtained as a halfway point between the upper and lower shelf energies, the stable crack propagation is followed by unstable crack propagation. A well-defined specific load, P_F, indicating the onset of unstable crack propagation and a load, P_A, for the fracture

arrest [15,35] can be distinguished in Fig. 3(a). The deflection is significantly larger than half of the impact specimen size. Some specimens do not separate into two pieces. Therefore, the Charpy V-notch impact energy above 190 J/cm^2 (Fig. 3b) is attributed to the fracture arrest in the present 10% Cr steel. At temperatures below the DBTT in the transition region II, the onset of unstable crack propagation occurs right after the maximum load is attained. The fracture arrest is not observed. The cracks propagate directly across the central portions of the impact test bars, and the total deflections below 6 mm are indicative of an advanced crack propagation rate relative to the velocity of the pendulum [11,35,36]. Thus, the DBTT obtained as a halfway point between the upper and lower shelf energies divides the transition region II into the high-temperature region, in which the unstable crack can be arrested, and the low-temperature region, in which the initiated brittle fracture proceeds up to the separation of the Charpy V-notch specimens into two pieces. In addition, this high-temperature region is characterized by a rather large value of impact-absorbed energy as compared to the low-temperature region.

To reveal the difference in the energy partitioning of the present 10% Cr steel and P92-type steel the load-deflection curves for these two steels were compared at temperature of 0 °C that is just below the DBTT for 10% Cr steel (Fig. 3(a,c)). A ratio of the crack initiation and propagation energies in the present steel is significantly different from that in the P92-type steel (Fig. 3(a,c)). The crack initiation energies calculated as an area under the initial portion of the load-deflection curves until the maximum load, P_m, are 51 and 60 J for the present 10% Cr and P92-type steels, respectively. On the other hand, the stable crack propagation energies calculated as an area under the section of the curves between P_m and P_F points are 39 and 165 J, for the present 10% Cr and P92-type steels, respectively. Thus, lowering the N and increasing the B contents decreases significantly the stable crack propagation energy by a factor of ~4.

Absorbed energy-deflection curves in Fig. 3(b) suggest that blunting of cleavage cracks takes place at temperatures above 10 °C, whereas intrinsic brittleness without crack blunting appears at lower temperatures. This critical temperature of 10 °C corresponds to the DBTT obtained as a halfway point between the upper and lower shelf energies. At temperatures above the DBTT, the blunting mechanism operates during unstable crack propagation, when the propagation of a cleavage crack induces the emission of dislocation ahead of fracture tip in a slip plane intersecting the cleavage plane. Increasing the temperature promotes this process that ceases the unstable crack propagation at 80 °C.

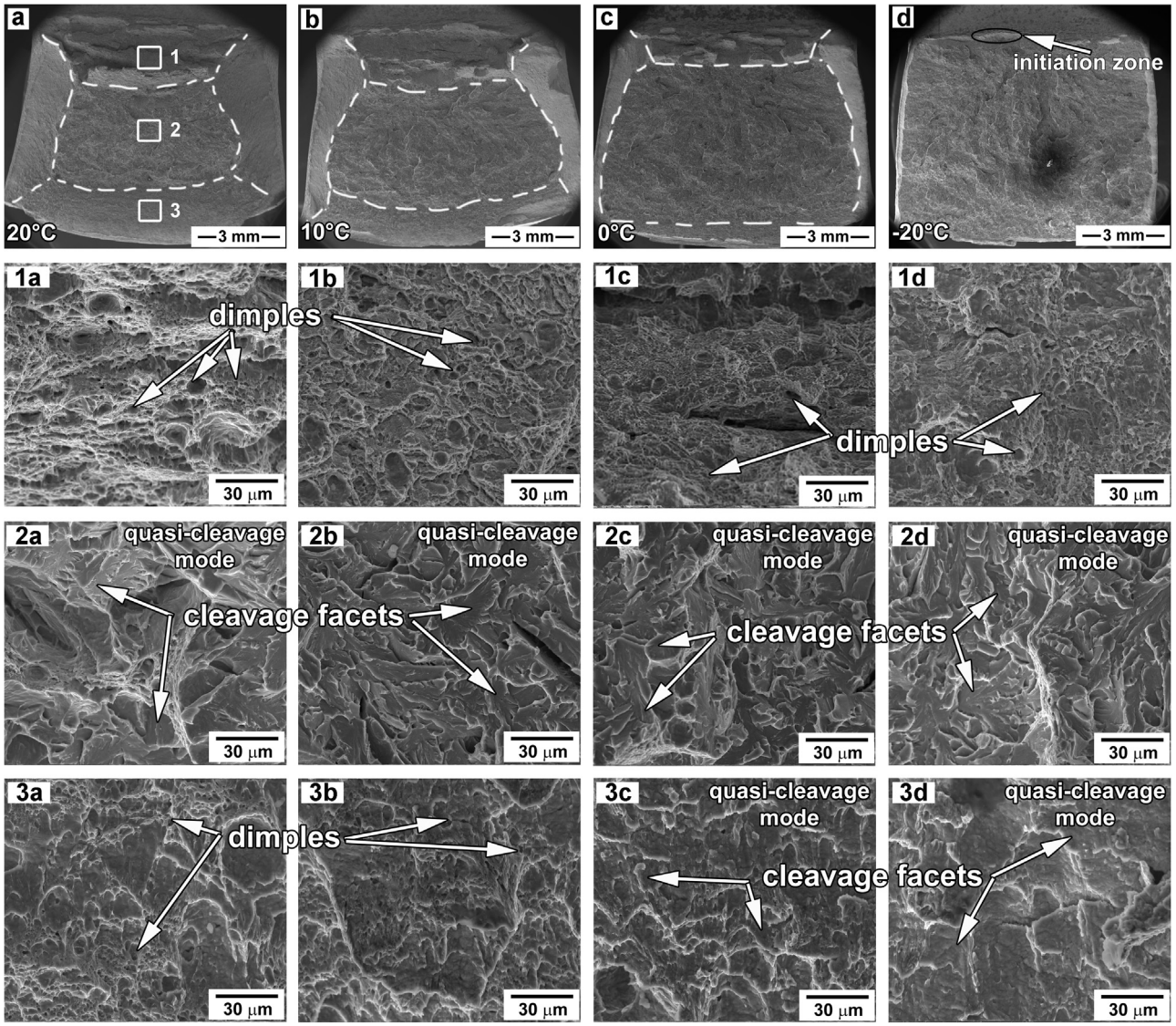

Fig. 4. Macrographs showing low-magnification general view (a-d) of the fracture surface in the Charpy V-notch specimens tested at: 20 °C (a); 10 °C (b); 0 °C (c); − 20 °C (d). SEM (secondary electron) fractographs showing high-magnification view of the crack initiation/stable crack propagation zone (1a-1d); (center) the unstable crack propagation zone (2a-2d), and the shear-lip zone (3a-3d).

Table 1
Sizes (mm) of fracture zones determined on SEM fractographs along a line normal to the notch mid-distance for the 10% Cr steel (numerator) / and P92-type steel [6] (denominator).

Zone	Test temperature, °C							
	20	10	0	− 10	− 20	− 40	− 65	− 80
Initiation zone	0.43 / 0.2	0.25	0.18	0.17	0.14 / 0.13	0.1	— / 0.34	0.1
Fibrous zone	2.7 / 6.10	1.88	1.48	1.11	0.48 / 3.93	0.24	— / 1.84	0
Unstable crack zone	2.8 / 0	4.22	5.7	6.42	6.75 / 3.33	7.5	— / 5.73	8.2
Shear-lip zone	2.16 / 2.28	1.6	0.84	0.46	0.46 / 1.2	0.36	— / 0.5	0
Total	8.09 / 8.51	7.95	8.2	8.16	7.83 / 8.6	8.2	— / 8.4	8.3

In the P92-type steel [6], the temperature, at which the transition to intrinsic brittleness owing to unstable crack propagation occurs, is 40 K higher than the DBTT obtained as a halfway point between the upper and lower shelf energies.

3.3. Fractography

Fig. 4 shows the low-magnification fractographs of the V-notch Charpy specimens after impact tests at temperatures between − 40 and 20 °C. The fracture surfaces consist of the initiation zone, the fibrous zone of stable crack propagation, the unstable crack propagation zone and the shear-lip zone of arrested crack propagation similar to other studies in the field [6,7,35,36]. Dimensions of these zones are summarized in Table 1 and their location is indicated in Fig. 4(a). The unstable crack propagation zone occupies a major portion of the fracture surface at all temperatures in Fig. 4. The narrow fibrous zone is surrounded by the initiation and extended shear-lip zones at room temperature (Fig. 4(a)). Decreasing the temperature expands the unstable crack propagation zone and reduces the initiation/fibrous zone ratio and the shear-lip zone (Fig. 4(b-d), Table 1). Stable crack propagation occurs in the ductile and transgranular manner in the fibrous zone (Fig. 4 (1a-1d)). The coarse and deep dimples alternate with shallow and fine dimples in the fibrous zone. The main feature of the fracture surfaces is the appearance of a well-defined unstable crack propagation zone (Fig. 4(2a-2d)). The unstable crack propagation occurring in a brittle manner through a quasi-cleavage fracture mode is arrested in the shear-lip zone by a sequential transition from the quasi-cleavage to ductile fracture with a fine-dimpled surface at 10...20 °C (Fig. 4(3a-3b)). This shear-lip zone becomes narrow and poorly defined because of quasi-cleavage domination at 0 °C (Fig. 4(c), Table 1). It is worth noting that at temperatures below 0 °C, the shear-lip zone is not observed. Therefore, the arrest of unstable crack propagation does not occur (Fig. 4(3c-3d)). The respective fracture surfaces consist of approximately 100 μm initiation zones and large unstable crack propagation zones (Table 1, Fig. 4(d)).

The present 10% Cr steel is tough at the DBTT. Following the crack initiation, subcritical cracks propagate in a stable manner for relatively long distances, and the unstable crack propagation is effectively hampered in the shear-lip zone. The extended initiation stage provides toughness above 28 J despite the short-distance stage of stable crack propagation in the temperature interval of − 20...0 °C. The embrittlement correlates with the disappearance of the fibrous and shear-lip zones at temperatures below − 20 °C. The onset of unstable crack propagation occurs immediately at the general yielding. At 28 J transition temperature, therefore, the toughness of the present 10% Cr steel is associated with the achievement of subcritical cracks at general yielding.

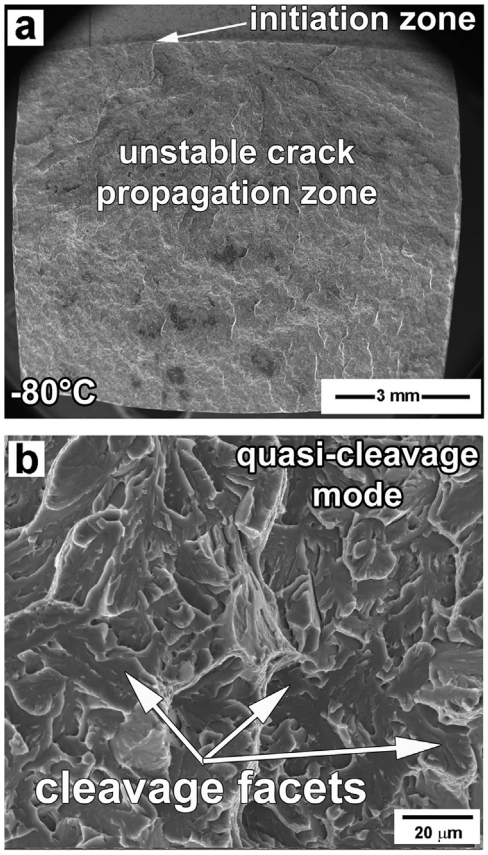

Fig. 5. Macrographs showing (a) low-magnification general view; (b) high-magnification view of the center of Charpy V-notch impact specimen tested at − 80 °C.

A decrease in temperature below − 80 °C strongly decreases the critical dimension of the crack susceptible to unstable propagation. The onset of unstable crack propagation occurs at the initiation stage (Figs. 4 and 5). The V-notch plays the role of a crack that may propagate in an unstable manner with negligible initiation stage (Fig. 5(a)). The steel becomes fully brittle at these temperatures, despite the quasi-cleavage transgranular fracture (Fig. 5(b)). Thus, the embrittlement is attributed to the approach of the subcritical dimension of unstable crack propagation front to the dimension of the created flaw.

Fig. 6 shows the side views of the unstable crack propagation zones of the Charpy specimens tested at temperatures of 10, − 20 and − 80 °C. The EBSD maps clearly reveal that a crack propagates through ferritic matrix across the numerous laths on the common cleavage planes at all studied temperatures, hence, confirming transgranular fracture. Cleavage in steels with bcc lattice is known to occur along its cubic planes {100} [15,17,19,37]. Almost flat surface of crack propagation occurs within a block, whereas the rugged surfaces are observed for different blocks, packets and PAGs. This indicates that the fracture surfaces are determined by the angle between {100} cleavage planes in neighbor blocks/packets. The crack changes the path propagation at HABs (Fig. 6). When the crack passes through a grain boundary, it has to propagate in a grain with a different orientation of {100} cleavage plane. As a result, the crack propagation path changes from a {100} cleavage plane to the other one. A quasi-cleavage fracture occurs due to the existence of packet or block boundaries playing a role of obstacles redirecting the crack propagation in a cleavage manner.

4. Discussion

Decreasing the N content and increasing the B content affects negatively DBT. Namely, the DBTT, 28 J and 6 J transition temperatures

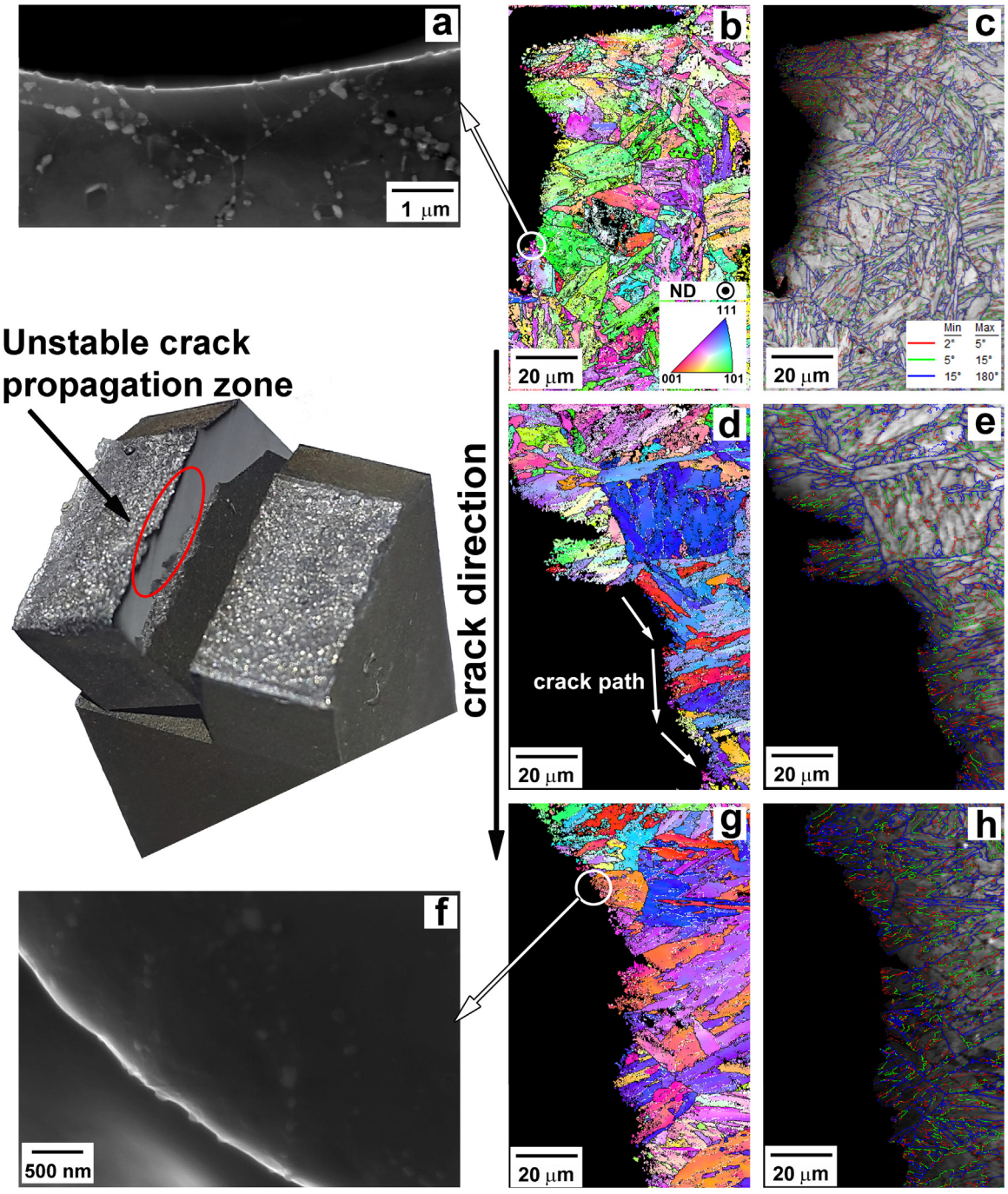

Fig. 6. Side-view SEM (secondary electron) images (a, f), OIM maps (b, d, g) and band contrast images (c, e, h) of the unstable crack propagation zone for the 10% Cr steel tested at (a, b, c) 10 °C; (d, e) 20 °C; (f, g,h) − 80 °C. White and black lines correspond to boundaries with misorientations of $2^\circ \le \theta < 15^\circ$ and $\ge 15^\circ$, respectively (b, d,g).

Table 2
Structural parameters for the 10% Cr and P92-type [6] steels.

Steel	Volume fraction of particles, (F_{VB}), %	Mean size of particles, nm	Lath width, nm	Density of particles, (β), μm^{-1}	Volume fraction of voids in the stable crack propagation zone, %
10% Cr	2.05	60	400	2.18	2.9
P92-type	1.78	85	400	0.94	0.7

in the present 10% Cr steel are significantly higher than those in steels with conventional 0.05% N-0.003% B contents [5–9,13]. Moreover, the unstable crack propagation in the intrinsic brittleness manner may occur at a relatively high temperature of 0 °C. On the other hand, the upper shelf energy for the present 10% Cr steel is slightly higher than those for conventional high-chromium steels [5–9,13]. It should be noted that an increase in the DBTT up to + 10 °C is not critical, because this value lies within the acceptance limit. The 28 J transition temperatures is − 27 °C, allowing the use of this steel for critical components of fossil power plants. However, precipitation of Laves phase at boundaries of TMLS under creep/aging conditions may significantly decrease the room-temperature fracture toughness below 40 J/cm^2

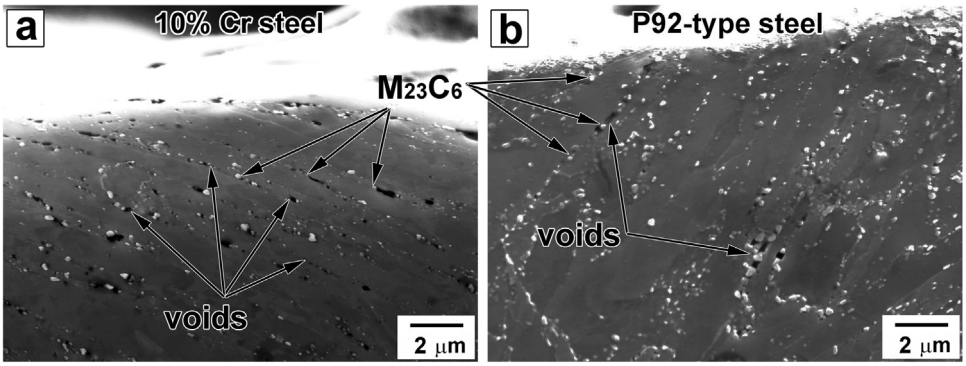

Fig. 7. Side-view SEM images (secondary electron) of the zone of stable crack propagation for the 10% Cr steel impact tested at 10 °C (a) and a P92-type steel impact tested at 20 °C (b).

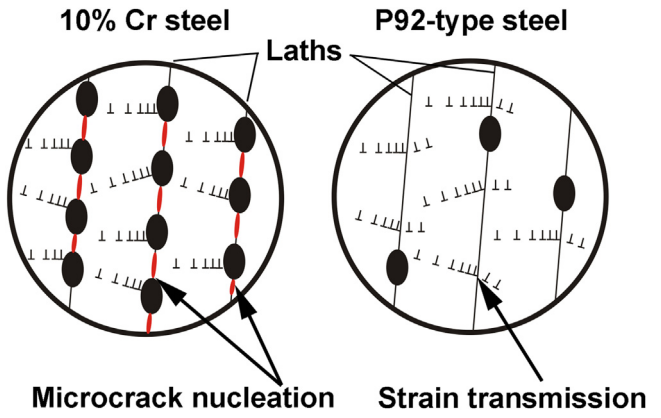

Fig. 8. Schematic illustration showing the stress relaxation by microcrack nucleation near carbides in the present 10% Cr steel and by strain transmission from lath to lath in the P92-type steel.

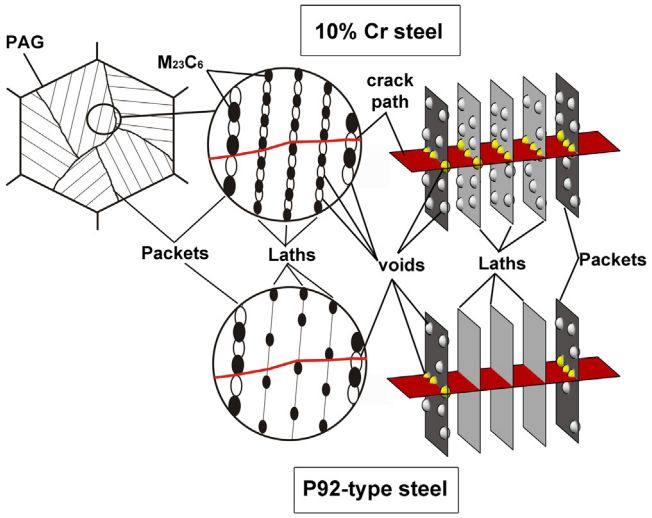

Fig. 9. Schematic illustration showing the void distribution in vicinity of the principal crack tip in the stable crack propagation zone for the present 10% Cr and P92-type steels.

[14,30]. Thus, the high-chromium steels with low N and high B contents could be susceptible to embrittlement under service condition.

The DBTT and the crack propagation modes in the present 10% Cr steel are remarkably different from those in conventional P92-type steels as described in Section 3.2. The crack initiation energies for both the present steel and P92-type steel are nearly the same, whereas the stable crack propagation energy for the latter significantly exceeds this energy for the former. The stage of crack initiation includes the achievement of the general yield load, P_{GY}, which corresponds to the extension of the plastic zone to the opposite surface of the specimen, i.e. the zone of plastic deformation appears at the tip of notch during impact test before crack propagation. The length of the fibrous zone in the P92-type steel exceeds that in the present 10% Cr steel by approximately 3–5 times at the same temperatures, although the dimensions of these zones at the DBTTs, i.e., at 10 °C and − 63 °C for the present 10% Cr and P92-type steels, respectively, are the same and comprise approximately 1.8–1.9 mm. (Table 1). Therefore, the difference in the DBTTs for these steels is attributed to different lengths of fibrous zone.

We suggest that the change in the lengths of fibrous zone is caused by difference in the steel microstructure and distribution of precipitations. The grain size significantly affects the DBTT and the grain growth shifts the transition temperature to higher values and reduces the impact toughness [7,8,13,38]. Though the present 10% Cr steel has an approximately 1.75 times larger the mean PAG size than the P92-type steel, the difference between grain sizes of 35 and 20 μm seems to be insufficient to change the DBBT remarkably. Moreover, the mean distances between HABs, characterizing the mean size of blocks, in these steels are identical. The same values of hardness (220 HB) also suggest similarity of TMLS in these steels. So, an increase in the DBTT in the present 10% Cr steel is not associated with slightly larger PAG size. This is in accordance with the results of Chatterjee et al. [8] inferring that PAG size may not be the determining factor in the ferritic-martensitic steels.

On the other hand, the change in the precipitate dispersion seems to be more important factor affecting the toughness of the present 10% Cr steel. To understand the effect of precipitates on the DBTT, the crack propagation mode, and the length of fibrous zone, let us consider the carbide precipitation (by Thermo-Calc calculation) and analyze the structure in vicinity of principal crack in the zone of stable crack propagation by SEM in the present 10% Cr steel and the P92-type steel. According to Thermo-Calc, the volume fractions, F_{vB}, of $M_{23}C_6$ carbides in the tempered 10% Cr and P92-type steels comprise 2.05% and 1.78%, respectively. Carbides precipitate during tempering on boundaries of laths, blocks, packets, and PAGs. The volume fraction of particles can be evaluated as [34,39]:

$$F_{vB} = \frac{\pi d^2 \beta}{3D} \quad (1)$$

where β is the density of particle distribution (particle density), D is the size of structural elements, i.e., the lath thickness taking into account that lath is the finest structural element in TMLS, and d is the size of particles. The particle density can be evaluated as:

$$\beta = \frac{3DF_{vB}}{\pi d^2} \quad (2)$$

Thus, the density of boundary carbides in the present 10% Cr steel

has been determined as 2.18 μm^{-1}, that is approximately 2.3 times greater than that of 0.94 μm^{-1} in the P92-type steel (Table 2). This corresponds with the structural observations of more dense chains of carbides on the lath boundaries in the tempered 10% Cr steel (Fig. 1) comparing to the P92-type steel, where $M_{23}C_6$ carbides at lath boundaries are rarely observed [6,31].

The side views of the Charpy specimens of the present 10% Cr steel and P92-type steel fractured at nearly the same temperatures of 10 and 20 °C, respectively, in the stable crack propagation region are shown in Fig. 7. The distinct difference in the microvoid formation in these steels is clearly seen in Fig. 7. The voids are evolved at the boundary carbides in both steels, whereas the density of distribution of these voids in the present 10% Cr steel is evidently higher (Fig. 7(a)) as compared to the P92-type steel (Fig. 7(b)). The volume fractions of the voids in the present 10% Cr steel and P92-type steel comprise approximately 2.9% and 0.7%, respectively. An abundant void formation occurs on all the types of boundaries including lath boundaries in the present 10% Cr steel (Fig. 7(a)), whereas the voids are mainly observed at HABs in the P92-type steel (Fig. 7(b)). Therefore, the presence of dense chains of $M_{23}C_6$ carbides at lath boundaries in the present 10% Cr steel substantially promotes the void formation on the boundary $M_{23}C_6$ carbides.

In its turn, the volume fraction of voids affects the dimension of the fibrous zone. It is well known that the principal crack serve as a stress concentration and the plastic deformation occurs in vicinity of principal crack tip [15,37]. The carbides located at lath boundaries serve as an effective barrier to the transmission of plastic deformation from one lath to another. Therefore, the lattice dislocations pile up against the carbides on laths boundaries (Fig. 8). As a result, high stresses at the heads of the pileups are relaxed by nucleation of numerous microcracks. These microcracks appear when there is no relaxation of the stresses by the strain transmission (dislocation motion over the barriers) [37]. The subsequent plastic deformation in the vicinity of microcrack tips leads to transformation of microcracks into the voids. As the principal crack length increases, the stress intensity factor increases. When the stress intensity factor attains the critical value the unstable crack propagation starts to occur by cleavage mode. Obviously, in the P92-type steel, plastic deformation transmits from lath to lath due to a low number of particles on the lath boundaries and the stress relaxation occurs by dislocation motion (Fig. 8). The void distribution in vicinity of the principal crack tip in the stable crack propagation zone for the present 10% Cr steel and P92-type steel is schematically shown in Fig. 9. The high density voids in the present 10% Cr steel facilitate the stable crack propagation. The numerous microcracks/voids at lath boundaries ahead of the principal crack tip serve as additional stress concentrations that increase the stress at the principal crack tip. Therefore, the stress in vicinity of the principal crack tip required for the onset of unstable crack propagation is attained in the present 10% Cr steel at smaller dimensions of the fibrous zone than in the P92-type steel. This is a reason for an increase in the DBTT of the 10% Cr steel containing low N and high B contents as compared to high-chromium steels with conventional 0.05% N-0.003% B contents.

5. Conclusions

The effect of the temperature on the impact toughness and fracture behavior of a 10% Cr-2% W-0.7% Mo-3% Co-0.05% Nb-0.2% V-0.008% B-0.003% N steel (all in wt%) was studied with the V-notch Charpy impact specimens tested at temperatures ranging from −196...100 °C. The main results are summarized as follows:

1. The present 10% Cr steel exhibits ductile-brittle transition (DBT). The DBT temperature (DBTT) determined as the temperature corresponding to a half of the sum of the upper and lower shelf energies (185 J/cm^2) is 10 °C, and the 28 J impact transition temperature is − 27 °C. Full embrittlement corresponding to an impact-absorbed energy of 6 J/cm^2 (6 J impact embrittlement temperature) appears at − 80 °C.
2. Decreasing the N content and increasing the B contents leads to an increase in the DBTT of the present 10% Cr steel as compared to high-chromium steels with conventional N and B contents because of high density of $M_{23}C_6$ carbides located at lath boundaries that provoke the intensive void formation and facilitate the formation of crack with critical dimension feasible for unstable propagation.

Acknowledgments

The study was financial supported by the Ministry of Education and Science of Russian Federation, under project of Government Task No. 11.2868.2017/PCh. The authors are grateful to Dr. A. Belyakov, Belgorod State University, for fruitful discussion of results. The authors are grateful to the staff of the Joint Research Center, "Technology and Materials", Belgorod State University, for providing the equipment for instrumental analysis.

References

[1] F. Abe, T.-U. Kern, R. Viswanathan, Creep-Resistant Steels, Woodhead Publishing, Cambridge, 2008.
[2] R.O. Kaybyshev, V.N. Skorobogatykh, I.A. Shchenkova, New martensitic steels for fossil power plant: creep resistance, Phys. Metal. Metallogr. 109 (2010) 186–200.
[3] A. Fedoseeva, N. Dudova, R. Kaibyshev, Role of tungsten in the tempered martensite embrittlement of a modified 9 pct Cr steel, Metall. Mater. Trans. A 48 (2017) 982–998.
[4] A. Kipelova, A. Belyakov, V. Skorobogatykh, I. Shchenkova, R. Kaibyshev, Tempering-induced structural changes in steel 10Kh9K3V1M1FBR and their effect on the mechanical properties, Met. Sci. Heat. Treat. 52 (2010) 100–110.
[5] M.V. Odnobokova, A.Yu Kipelova, A.N. Belyakov, R.O. Kaibyshev, Mechanical behavior and brittle–ductile transition of high-chromium martensitic steel, Phys. Metal. Metallogr. 117 (2016) 390–398.
[6] V. Dudko, A. Fedoseeva, R. Kaibyshev, Ductile-brittle transition in a 9% Cr heat-resistant steel, Mater. Sci. Eng. A 682 (2017) 73–84.
[7] A. Chatterjee, D. Chakrabarti, A. Moitra, R. Mitra, A.K. Bhaduri, Effect of normalization temperatures on ductile brittle transition temperature of a modified 9Cr–1Mo steel, Mater. Sci. Eng. A 618 (2014) 219–231.
[8] A. Chatterjee, A. Moitra, A.K. Bhaduri, D. Chakrabarti, R. Mitra, Effect of heat treatment on ductile–brittle transition behavior of 9Cr–1Mo steel, Procedia Eng. 86 (2014) 287–294.
[9] A. Chatterjee, D. Chakrabarti, A. Moitra, R. Mitra, A.K. Bhaduri, Effect of deformation temperature on the ductile–brittle transition behavior of a modified 9Cr–1Mo steel, Mater. Sci. Eng. A 630 (2015) 58–70.
[10] K.C. Sahoo, J. Vanaja, P. Parameswaran, V.D. Vijayanand, K. Laha, Effect of thermal ageing on microstructure, tensile and impact properties of reduced activated ferritic-martensitic steel, Mater. Sci. Eng. A 686 (2017) 54–64.
[11] A. Chatterjee, A. Moitra, A.K. Bhaduri, R. Mitra, D. Chakrabarti, Dynamic fracture behaviour of thermo-mechanically processed modified 9Cr–1Mo steel, Eng. Fract. Mech. 149 (2015) 74–88.
[12] S. Sathyanarayanan, J. Basu, A. Moitra, G. Sasikala, V. Singh, Effect of thermal aging on ductile-brittle transition temperature of modified 9Cr-1Mo steel evaluated with reference temperature approach under dynamic loading condition, Metall. Mater. Trans. A 44 (2013) 2141–2155.
[13] X. Hu, L. Huang, W. Yan, W. Wang, W. Sha, Y. Shan, K. Yang, Evolution of microstructure and changes of mechanical properties of CLAM steel after long-term aging, Mater. Sci. Eng. A 586 (2013) 253–258.
[14] W. Zhong, W. Wang, X. Yang, W. Li, W. Yan, W. Sha, W. Wang, Y. Shan, K. Yang, Relationship between Laves phase and the impact brittleness of P92 steel re-evaluated, Mater. Sci. Eng. A 639 (2015) 252–258.
[15] ASM Handbook: Mechanical Testing and Evaluation 8 ASM International, 2000, p. 2235.
[16] A. Pineau, Modeling ductile to brittle fracture transition in steels—micromechanical and physical challenges, Int. J. Fract. 150 (2008) 129–156.
[17] G. Krauss, Steels: Processing, Structure, and Performance, ASM International, USA, 2005.
[18] A. Das, Fracture complexity of pressure vessel steels, Philos. Mag. 97 (2017) 3084–3141.
[19] A. Pineau, A.A. Benzerga, T. Pardoen, Failure of metals I: brittle and ductile fracture, Acta Mater. 107 (2016) 424–483.
[20] H. Kitahara, R. Ueji, N. Tsuji, Y. Minamino, Crystallographic features of lath martensite in low-carbon steel, Acta Mater. 54 (2006) 1279–1288.
[21] H. Semba, F. Abe, Alloy design and creep strength of advanced 9%Cr USC boiler steels containing high concentration of boron, Energy Mater. 1 (2006) 238–244.
[22] M. Tabuchi, H. Hongo, F. Abe, Creep strength of dissimilar welded joints using high B-9Cr steel for advanced USC boiler, Metall. Mater. Trans. A 45 (2014) 5068–5075.
[23] Y. Liu, S. Tsukamoto, K. Sawada, M. Tabuchi, F. Abe, Precipitation behavior in the heat-affected zone of boron-added 9Cr-3W-3Co steel during post-weld heat treatment and creep deformation, Metall. Mater. Trans. A 46 (2015) 1843–1854.
[24] N. Dudova, R. Mishnev, R. Kaibyshev, Effect of tempering on microstructure and

mechanical property of boron containing 10%Cr Steel, ISIJ Int. 51 (2011) 1912–1918.
[25] R. Mishnev, N. Dudova, A. Fedoseeva, R. Kaibyshev, Microstructural aspects of superior creep resistance of a 10%Cr martensitic steel, Mater. Sci. Eng. A 678 (2016) 178–189.
[26] R. Sahara, T. Matsunaga, H. Hongo, M. Tabuchi, Theoretical investigation of stabilizing mechanism by boron in body-centered cubic iron through $(Fe,Cr)_{23}(C,B)_6$ precipitates, Metall. Mater. Trans. A 47 (2016) 1–11.
[27] N. Dudova, R. Kaibyshev, On the precipitation sequence in a 10%Cr steel under tempering, ISIJ Int. 51 (2011) 826–831.
[28] L. Li, R. Maclachlan, M.A.E. Jepson, R. Thomson, Microstructural evolution of boron nitride particles in advanced 9Cr power plant steels, Metall. Mater. Trans. A 44 (2013) 3411–3418.
[29] P. Yan, Zh Liu, H. Bao, Y. Weng, W. Liu, Effect of tempering temperature on the toughness of 9Cr–3W–3Co martensitic heat resistant steel, Mater. Des. 54 (2014) 874–879.
[30] P. Yan, Zh Liu, Toughness evolution of 9Cr-3W-3Co martensitic heat resistant steel during long time aging, Mater. Sci. Eng. A 650 (2016) 290–294.
[31] V. Dudko, A. Belyakov, D. Molodov, R. Kaibyshev, Microstructure evolution and pinning of boundaries by precipitates in a 9 pct Cr heat resistant steel during creep, Metall. Mater. Trans. A 44 (2013) 162–172.
[32] ASTM E23-05, Standard test methods for notched bar impact testing of metallic materials, Annual Book of ASTM Standards, 03.01, ASTM International, Pennsylvania, USA, 2005.
[33] R. Kaibyshev, R. Mishnev, E. Tkachev, N. Dudova, Effect of Ni and Mn on the creep behaviour of 9–10%Cr steels with low N and high B, Trans. Indian Inst. Met. 69 (2016) 203–210.
[34] R. Mishnev, N. Dudova, R. Kaibyshev, On the origin of the superior long-term creep resistance of a 10%Cr steel, Mater. Sci. Eng. A 713 (2018) 161–173.
[35] R. Chaouadi, A. Fabry, On the utilization of the instrumented Charpy impact test for characterizing the flow and fracture behavior of reactor pressure vessel steels, in: D. Francois, A. Pineau (Eds.), From Charpy to Present Impact Testing, Elsevier Science Ltd. and ESIS, Oxford, UK, 2002, pp. 103–117.
[36] ASM Handbook, Fractography 12 ASM International, 1987, p. 857.
[37] M.A. Meyers, K.K. Chawla, Mechanical Behavior of Materials, Cambridge University Press, USA, 2009.
[38] H. Qiu, T. Hanamura, S. Torizuka, Influence of grain size on the ductile fracture toughness of ferritic steel, ISIJ Int. 54 (2014) 1958–1964.
[39] N. Dudova, A. Plotnikova, D. Molodov, A. Belyakov, R. Kaibyshev, Structural changes of tempered martensitic 9%Cr–2%W–3%Co steel during creep at 650 °C, Mater. Sci. Eng. A 534 (2012) 632–639.